

Manuscript version: Author's Accepted Manuscript

The version presented in WRAP is the author's accepted manuscript and may differ from the published version or Version of Record.

Persistent WRAP URL:

<http://wrap.warwick.ac.uk/115804>

How to cite:

Please refer to published version for the most recent bibliographic citation information. If a published version is known of, the repository item page linked to above, will contain details on accessing it.

Copyright and reuse:

The Warwick Research Archive Portal (WRAP) makes this work by researchers of the University of Warwick available open access under the following conditions.

Copyright © and all moral rights to the version of the paper presented here belong to the individual author(s) and/or other copyright owners. To the extent reasonable and practicable the material made available in WRAP has been checked for eligibility before being made available.

Copies of full items can be used for personal research or study, educational, or not-for-profit purposes without prior permission or charge. Provided that the authors, title and full bibliographic details are credited, a hyperlink and/or URL is given for the original metadata page and the content is not changed in any way.

Publisher's statement:

Please refer to the repository item page, publisher's statement section, for further information.

For more information, please contact the WRAP Team at: wrap@warwick.ac.uk.

Autonomous Landing Control of Highly Flexible Aircraft based on Lidar Preview in the Presence of Wind Turbulence

Pengyuan Qi¹, Xiaowei Zhao^{1*} and Rafael Palacios²

Abstract—This paper investigates preview-based autonomous landing control of a highly flexible flying wing model using short range Lidar wind measurements in the presence of wind turbulence. The preview control system is developed based on a reduced-order linear aeroelastic model and employs a two-loop control scheme. The outer loop employs the LADRC (linear active disturbance rejection control) and PI algorithms to track the reference landing trajectory and vertical speed, respectively, and to generate the attitude angle command. This is then used by the inner-loop using H_∞ preview control to compute the control inputs to the actuators (control flaps and thrust). A landing trajectory navigation system is designed to generate real-time reference commands for the landing control system. A Lidar (light detection and ranging) simulator is developed to measure the wind disturbances at a distance in front of the aircraft, which are provided to the inner-loop H_∞ preview controller as prior knowledge to improve control performance. Simulation results based on the full-order nonlinear flexible aircraft dynamic model show that the preview-based landing control system is able to land the flying wing effectively and safely, showing better control performance than the baseline landing control system (without preview) with respect to landing effectiveness and disturbance rejection. The control system's robustness to measurement error in the Lidar system is also demonstrated.

Index Terms—Highly flexible aircraft, autonomous landing control, turbulence landing, H_∞ preview control, Lidar wind measurements.

I. INTRODUCTION

Modern aircraft design is pursuing higher efficiency by employing light weight materials and high aspect-ratio wings, which results in a more flexible airframe. Particular interest are the High Altitude Long Endurance Unmanned Aerial Vehicles (HALE UAVs), which have shown potential advantages in achieving the efficiency targets and undertaking a wide range of military and civilian missions [1]. This class of aircraft may exhibit large structural deformations during flight due to high flexibility. The resulting strong couplings between structural dynamics, aerodynamics and flight dynamics pose great challenges in terms of airframe modeling and dynamic control [2–10]. Moreover, highly flexible aircraft are much more sensitive to atmospheric disturbances, therefore active aeroelastic control is typically required for gust load alleviation

and disturbance rejection [11–14]. Some works on trajectory control of such aircraft [15–17] have also been undertaken recently, while some key challenging scenarios, such as autonomous landing control, have rarely been investigated.

As a critical flight phase, landing determines whether an aircraft can be safely recovered. Statistics show that nearly half of the aircraft accidents occur during landing [18], and autonomous landing in the presence of atmospheric disturbance (such as windshears, crosswinds, etc.) is still one of the current bottlenecks in large UAV development. For example, the HALE UAV Aquila developed by Facebook was reported to be substantially damaged in a crash due to sudden wind gusts in the landing phase [19]. These all imply the demand for more effective method in aspect of autonomous landing control of highly flexible aircraft. Current research on landing control is mostly devoted to rigid-body aircraft [20–26] and has rarely touched flexible ones. Hoseini et.al. [27] developed a landing control system for a simple flexible aircraft based on LQR/integral/feedforward closed-loop control. They employed LQR control to track the landing commands with an integrator to eliminate the steady-state error and a feedforward controller to reduce the effects of disturbances (which were assumed to be measurable). The control system could steer the aircraft through the landing path successfully in the presence of constant crosswinds. However, the controller required full state feedback and did not consider turbulent wind. Their nonlinear aircraft model was also relatively stiff.

The contribution of this paper is to investigate the autonomous landing control of highly flexible aircraft, using Lidar (light detection and ranging) preview to improve control performance in the presence of wind turbulence. Lidar can be used to measure the line-of-sight (LOS) component of the approaching wind disturbances at a distance ahead of the aircraft by detecting the Doppler shift in atmospheric backscatter [28]. With specific scanning pattern, one is able to retrieve the three-dimensional velocity components [29], which can be provided to the control system as preview knowledge. In this manner, the preview controller has access to the time-advanced measurement of wind disturbances in addition to the feedback signals on the aircraft state [30]. This enables the preview control system to act before the wind disturbances actually affect the aircraft, therefore improves the control performance, which can largely benefit the autonomous landing control of highly flexible aircraft.

Preview control with Lidar wind measurements have been widely used in wind turbine control [31–33]. For their applica-

¹P. Qi and X. Zhao are with the School of Engineering, University of Warwick, Coventry CV4 7AL, United Kingdom, email: {P.Qi, Xiaowei.Zhao}@warwick.ac.uk (*Corresponding author: Xiaowei Zhao.)

²R. Palacios is with the Department of Aeronautics, Imperial College London, London SW7 2AZ, United Kingdom, email: r.palacios@imperial.ac.uk

tions in flight control, Rabadan et.al. [34] developed and flight-tested an airborne forward-looking Lidar system on an Airbus A340-300 testbed. Flight-test measurements showed that the designed Lidar system was potential for future implementation in a real-time feedforward flight control system. The work of [35–37] investigated the gust load alleviation (GLA) problem using Lidar preview measurements of the incoming gust, based on model predictive control, gain-scheduled linear parameter-varying control and adaptive feedforward control, respectively. Their simulation results showed that the wing root bending moments and the average vertical acceleration were largely reduced, indicating better load alleviation performance and disturbance rejection performance. In addition to Lidar wind measurements, Hesse and Palacios [38] investigated the GLA problem for flexible aircraft in wake vortex encounters, where the gust is assumed to be measured at the aircraft nose by a 5-hole probe and used as prior information. Simulation results showed that the combined feedforward/feedback H_∞ controller and the use of direct lift control surfaces obtained significant load reductions.

As mentioned earlier, we aim to investigate the autonomous landing control based on Lidar preview for the large highly flexible flying wing developed in [4]. Its aeroelastic and trajectory control (without preview) was studied in [17], which used a two-loop control structure in each of the longitudinal and lateral channels to realize efficient trajectory tracking. The outer loop employed the PI/LADRC (linear active disturbance rejection control) algorithms to track the desired trajectory and generate attitude angle command to the inner loop, based on which the inner loop used H_∞ control technique to compute the control inputs to the corresponding control actuators. To achieve preview-based landing control, in the present paper we extend the inner-loop H_∞ control structure in [17] by introducing Lidar preview wind measurements to the controller as prior information. We design a Lidar simulator to measure the incoming wind disturbances in the wind field, and then augment the plant model with the preview measurements through a discrete-time delay chain. We obtain the preview controller through discrete-time mixed sensitivity H_∞ synthesis [39] with the augmented plant model. A landing trajectory generator (navigation system) is also developed to generate real-time reference commands for the landing control system. Our control design is based on a reduced-order linear model (thus robustness of the controller is very important) while simulation is conducted based on the full-order nonlinear model. Simulation results show that the preview-based landing control system has achieved better landing effectiveness and disturbance rejection performance compared to the baseline landing control system (without preview) in the presence of wind turbulence, which realizes more efficient and safer autonomous landing.

The structure of this paper is as follows: Section II develops a landing trajectory generator to generate real-time reference commands for the landing control system. Section III develops a Lidar simulator to measure the three-dimensional velocity components of the incoming wind disturbances in the wind field. Section IV designs the preview-based landing control system using a two-loop PI/LADRC and H_∞ preview control

scheme for the highly flexible flying wing model and Section V conducts simulation studies to test the performance of the control system. Section VI concludes this paper.

II. LANDING TRAJECTORY DESIGN

This work assumes the wheeled landing recovery method. This means that the aircraft tracks a pre-defined descent trajectory and touches down near the desired touchdown point with appropriate speed and attitude angle, which requires an efficient and robust autonomous landing control system. Normally, the landing process consists of three main phases, the final approach phase, the flare phase and the taxi phase. As illustrated in Fig. 1, when the flying wing descends to a pre-defined altitude H_0 and is commanded to land, it enters the final approach phase where it glides down quickly in uniform linear motion at constant flight path angle γ . Then as the flying wing glides down to the pre-defined altitude H_1 , it enters the flare phase where it descends slowly with a gradual trajectory and simultaneously adjusts its vertical speed and attitude angle to guarantee safe touchdown at point O . The flying wing enters the taxi phase from point O , where it keeps slowing down and taxiing on the runway till stopping. Note that the midpoint of the flying wing is selected as reference point to track the altitude H and the flight path angle γ of the aircraft. In this paper, we focus on the in-air final approach and flare phases which are of crucial importance in autonomous landing.

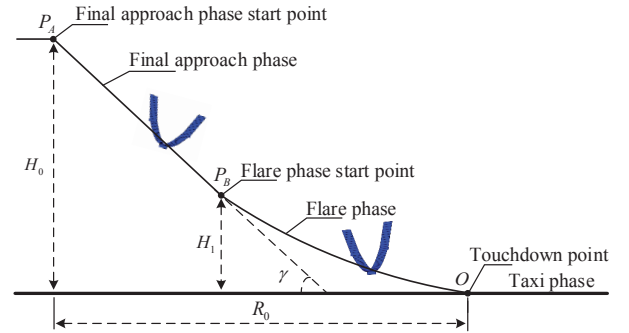


Fig. 1. Illustration of the landing process. R_0 is the projected distance from the final approach phase starting point P_A to the desired touchdown point O , respectively. γ is the descent flight path angle in the final approach phase.

In the longitudinal channel of the final approach phase, the landing trajectory of the aircraft is a straight line whose slope is determined by the descent flight path angle γ . The flying wing is desired to track this straight line, we define the altitude command for the final approach phase as

$$H_r(R) = H_0 + (R_0 - R) \tan \gamma + H_\Delta. \quad (1)$$

where R is the traveling distance since entering the final approach phase, $H_\Delta = k\gamma + b$ is a pre-compensator (depending on the flight path angle γ only) introduced to compensate the slow altitude response of the landing control system when tracking a time-dependent altitude command, such that the flying wing can follow the desired descent trajectory effectively in the final approach phase. With the designed landing control system, the parameters k and b are determined by the slope and intercept of the approximate linear equation

of the altitude tracking error and the descent flight path angle. While in the flare phase, the altitude is expected to be reduced exponentially. As employing altitude tracking in this phase may cause large pitch angle motion when approaching the ground in the presence of wind disturbances which increase the risk of structural impair, we employ vertical speed control instead of altitude tracking to ensure the aircraft achieves appropriate touch down speed and pitch angle for safe landing. Although this may cause the loss of touch down effectiveness in disturbance, the situation can be improved by the preview-based landing control system. Therefore, we define the vertical speed command for the flare phase as

$$\dot{H}_r(R) = v_{zr} + \frac{(v_{z0} - v_{zr})}{H_1} H, \quad (2)$$

where v_{z0} is the instantaneous vertical speed at the flare phase starting point, and v_{zr} is the desired vertical speed at the touchdown point. The forward velocity is required to maintain its trim value (i.e. $V_r = V_{trim}$) in both phases.

In the lateral channel, the trajectory of the flying wing is expected to align with the center of the runway in both the final approach and flare phases, the reference command for the lateral displacement (defined as the lateral deviation from current position to the center of the runway) is then simply given as $S_r = 0$. Combining all the reference commands above, a landing trajectory generator is designed to generate corresponding real-time reference commands for the landing control system, as shown in Fig. 2. The first three of the four commands are fed into the landing control system in the final approach phase while the last three of the four commands are utilised in the flare phase.

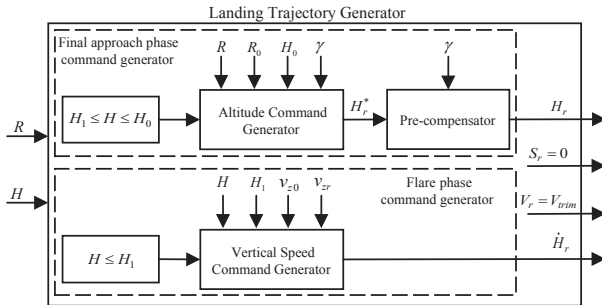


Fig. 2. Structure of the landing trajectory generator. Pre-defined parameters include the travelling distance since entering the final approach phase (R), the projected distance from the final approach phase starting point to the desired touchdown point (R_0), altitude of the final approach phase starting point (H_0) and the flare phase starting point (H_1), the descent flight path angle (γ) and the desired vertical speed at the touchdown point (v_{zr}). H is current altitude.

III. LIDAR SIMULATOR DESIGN

In this section, we design the Lidar simulator to measure the wind disturbances at a distance in front of the aircraft as prior knowledge for preview control design. We extend the Lidar simulator based on the work of [40] to measure the three-dimensional velocity components of the wind disturbances using Velocity Azimuth Display (VAD) technique.

A. Line-of-Sight Wind Measurement

Assuming that in the inertial reference frame the coordinates of the Lidar system fixed at the center of the flying wing are $[x_a, y_a, z_a]'$ and the coordinates of a measurement point i at a distance r_i in front of the Lidar system are $[x_i, y_i, z_i]'$. Given the actual wind velocity $[u_i, v_i, w_i]'$ at point i , we calculate its line-of-sight (LOS) component as

$$v_{los,i} = \int_{-\infty}^{\infty} (x_{n,i}(u_i - \dot{x}_a) + y_{n,i}(v_i - \dot{y}_a) + z_{n,i}(w_i - \dot{z}_a)) f_{rw}(a) da, \quad (3)$$

where $[x_{n,i}, y_{n,i}, z_{n,i}]'$ is the normalized laser beam vector from the Lidar system to the measurement point i , and $[\dot{x}_a, \dot{y}_a, \dot{z}_a]'$ is the instantaneous velocity of the Lidar system. f_{rw} is the normalized spatial weighting function as Lidar measures within the probe volume the beam intersects, as shown in Fig. 3.

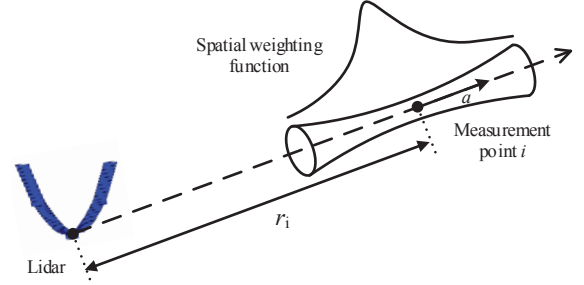


Fig. 3. Illustration of the line-of-sight measurement.

The spatial weighing function is given in the form of

$$f_{rw}(a) = \frac{1}{\eta_L \sqrt{2\pi}} \exp\left(-\frac{a^2}{2\eta_L^2}\right), \quad \eta_L = \frac{W_L}{2\sqrt{2\ln 2}}, \quad (4)$$

where a is the distance from the focus point along the laser beam. This effectively acts as a low-pass filter for the wind disturbance measurements which is helpful to preview control. We assume $r_i = 24.4m$ and $W_L = 10m$ in this paper.

B. Three-dimensional Wind Measurement

We now employ Velocity Azimuth Display (VAD) technique to retrieve the three-dimensional velocity components of the wind disturbances, assuming the uniform distribution of wind velocity at the same measurement range [41]. The Lidar system is designed to scan conically towards the forward direction at a fixed elevation angle φ , measuring the LOS wind velocity at a certain number of points with different azimuth angle λ_i , as depicted in Fig. 4. In this manner, we obtain a set of LOS measurement data which can fit into a sinusoidal/cosine function (see Fig. 5) as

$$v_{fit} = m + n \cos(\lambda - \lambda_{max}). \quad (5)$$

The actual LOS velocity component of measurements with respect to different azimuth angle λ are described as

$$v_{actual} = u_l \sin \varphi + v_l \cos \varphi \sin \lambda - w_l \cos \varphi \sin \lambda,$$

where $[u_l, v_l, w_l]'$ is the resultant velocity of the average wind velocity and the aircraft velocity. By setting $v_{actual} = v_{fit}$,

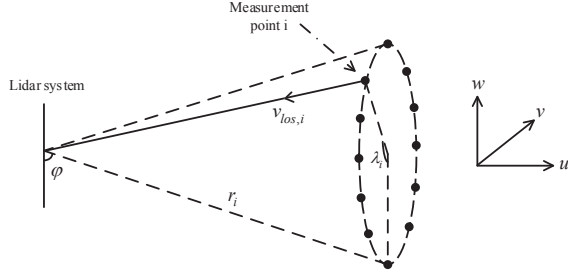


Fig. 4. Illustration of the Lidar scanning pattern. u, v, w are the respective mean value of the three-dimensional velocity components of wind disturbances at the measurement plane. The number of measurement points is 12 for the trade-off of measurement accuracy and real-time computational burden.

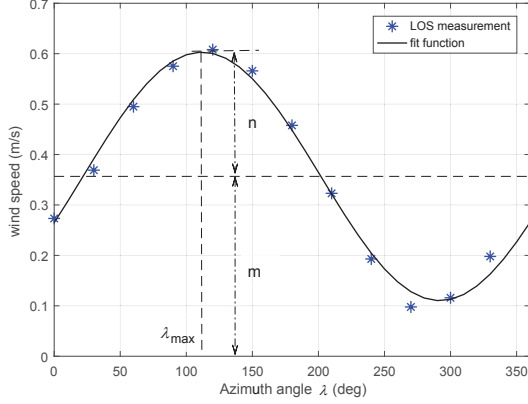


Fig. 5. Illustration of the measurement data fitting. The blue asterisks denote the set of LOS measurement data during a scanning cycle, the red solid line is the resulting fit function.

we get the respective mean value of the three-dimensional components of the resultant wind velocity as

$$\begin{cases} u_l = m / \sin \varphi, \\ v_l = n \sin \lambda_{\max} / \cos \varphi, \\ w_l = -n \cos \lambda_{\max} / \cos \varphi. \end{cases} \quad (6)$$

Assuming the wind disturbances travel with mean speed from the measurement location to the aircraft based on Taylor's Hypothesis of Frozen Turbulence [42], we obtain the mean value of the velocity of the wind disturbances as

$$\begin{cases} u = u_l - \dot{x}_a, \\ v = v_l - \dot{y}_a, \\ w = w_l - \dot{z}_a, \end{cases} \quad (7)$$

where $[\dot{x}_a, \dot{y}_a, \dot{z}_a]'$ is the velocity of the Lidar system, i.e. the velocity of the aircraft which can be measured by airborne sensors.

IV. CONTROL DESIGN

In this section, we design the preview-based landing control system based on a flying wing model developed in [14] as depicted in Fig. 6. We first briefly introduce this model.

A nonlinear aeroservoelastic model using intrinsic degrees of freedom (sectional inertial linear (v) and angular velocities (ω), resultant sectional forces (F) and moments (M)) and linear unsteady aerodynamics was developed in [14] to describe the

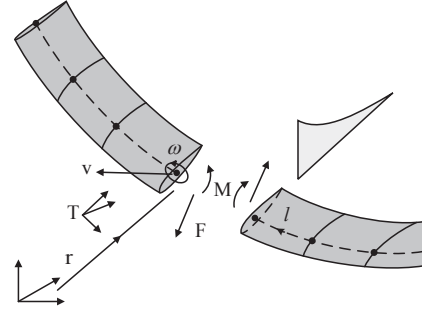


Fig. 6. Illustration of the very flexible flying wing.

coupled structural dynamics, aerodynamics and flight dynamics of the very flexible flying wing. Projection of that system on a modal basis gives

$$\begin{aligned} \dot{q}_s &= A_s q_s + \Gamma(q_s) q_s \\ &\quad + (H_1(q_s^*) + V_\infty H_2(q_a) + H_{3,a}(q_s^*) \delta_d) q_s^* \\ &\quad + H_g(q_s) T_0 + H_T f_T, \\ \dot{q}_a &= P_1 q_s^* - V_\infty P_2 q_a, \\ \dot{T}_0 &= T_0 N_1(q_s), \\ \dot{r}_0 &= T_0 N_2(q_s), \end{aligned} \quad (8)$$

where the full set of states include the structural states $q_s = [q_1, q_2]$ (q_1 and q_2 denote the modal amplitudes in sectional linear/angular velocities and force/moment resultants, respectively), the aerodynamic states q_a , the rigid-body orientation T_0 and the displacement vector r_0 of each node along the airframe beam in the inertial reference frame. $q_s^* = q_s + q_g$ where q_g is the gust velocity distribution projected onto the velocity modal basis. The matrix A_s and operator Γ describe the linear and geometrically-nonlinear dynamics of the aircraft, respectively. Linear operators H_1 and H_2 describe the modal projection of aerodynamic loads, while the operators H_g, H_3 and matrix H_T describe the effect of gravity, the aerodynamic forces caused by control surfaces and the engine thrust forces, respectively. Constant matrices P_1 and P_2 define the evolution of the aerodynamic lags with the amplitude of the structural modes, while the linear operators N_1 and N_2 serve to integrate the rotation matrix and displacement vector from the local velocities. The flap deflection angles δ_d and the engine thrust settings f_T are defined as control inputs. We refer to [14] for more details of the aircraft modeling.

The above modal description (8) requires a large number of states ($\mathcal{O}(10^3)$) for convergence in time-domain simulations. To make the size suitable for control design, the full-order nonlinear model (8) is linearized around a trim equilibrium and then reduced by balanced truncation. The resulting similarity transformation is written as $x = \mathbf{R}q$, where the projection matrix \mathbf{R} is obtained from system balancing, with an associated pseudo-inverse transformation \mathbf{R}^* defined from the reduction such that identity $\mathbf{R}\mathbf{R}^* = \mathbf{I}$ holds. Retaining the quadratic nonlinearities, we obtain the reduced-order nonlinear model,

$$\begin{aligned} \dot{x} &= (A_{fc} + Q(x))x + B_{fwd}d + B_{fuc}u_c, \\ y &= C_{fc}x, \end{aligned} \quad (9)$$

Discretizing the resulted system, modeling all control ac-

tuators as first-order lag systems (with time constant of 0.1s) and setting the Q terms to be zero lead to the discrete-time linear state space model

$$\begin{aligned} x(k+1) &= A_f x(k) + B_{fw} d(k) + B_{fu} u_c(k), \\ y(k) &= C_f x(k), \end{aligned} \quad (10)$$

which will be used for the control synthesis below.

As mentioned earlier, an aeroelastic and trajectory control system was designed in our paper [17] for this model to achieve efficient trajectory tracking in the presence of turbulence. We now extend the control system to achieve autonomous landing and include Lidar preview wind measurements (obtained in Section III) in the inner loop to benefit the landing scenario, as illustrated in Fig. 7. The introduction of such preview knowledge enables the control system to act before the wind disturbances impact the aircraft, thus improves landing effectiveness and disturbance rejection performance. Here, we mention again that we choose the midpoint of the flying wing as reference point to track the aircraft flight dynamics, thus all the variables in the following context are defined/measured at this reference point.

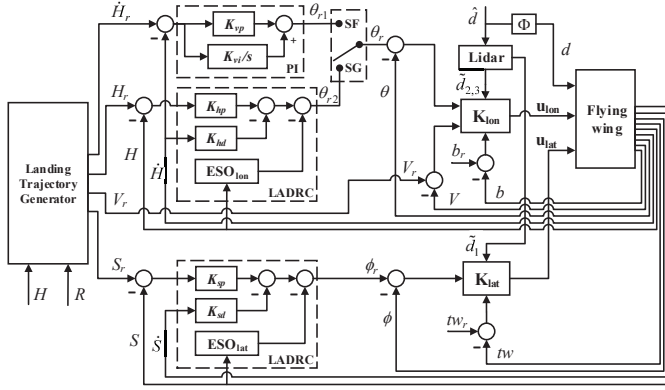


Fig. 7. Structure of the preview-based landing control system: the upper part is for the longitudinal channel while the lower part is for the lateral channel. Output feedback signals are altitude H , lateral displacement S , forward velocity V , pitch angle θ , roll angle ϕ , root bending moment b and twist moment tw . R is the traveling distance since entering the final approach phase. ESO_{lon} and ESO_{lat} are the extended state observers (ESO) in LADRC. \hat{d} is the actual wind disturbances at a distance in front of the aircraft, \tilde{d} is the Lidar wind measurements, d is the wind disturbances that actually impact the aircraft, and Φ is an N -step delay chain. K_{lon} and K_{lat} are the H_∞ preview controllers. The subscript symbol r denotes the reference command, while the \bullet symbol denotes time derivative. K_{hp} , K_{hd} , K_{sp} , K_{sd} , K_{vp} and K_{vi} are the corresponding controller parameters.

In the longitudinal channel during landing, when the flying wing descends to the altitude of the final approach phase starting point H_0 (see Fig. 1), the outer-loop controller is connected to SG “glide control” (see Fig. 7), driving the aircraft to glide down at constant flight path angle, which is achieved by LADRC altitude control to track the desired altitude command. Once the flying wing descends to the altitude of the flare phase starting point H_1 , the outer-loop controller is then connected to SF “flare control”, driving the aircraft to gradually adjust its vertical speed and pitch angle to the desired range to guarantee safe touchdown, which is achieved by PI vertical speed control. These outer-loop LADRC controller (using altitude and vertical speed as

feedback) and PI controller (using vertical speed as feedback) generate pitch angle command for the inner loop. We mention that to reduce the impact of gains during switch, the pitch angle command $\theta_{r,2}$ at switch is used as the initial value of the integral term in the PI controller. The H_∞ preview controller is designed in the inner loop to generate control inputs (to the corresponding longitudinal flaps and thrust) to track this pitch angle command and maintain the forward velocity at its trim value simultaneously, using pitch angle, forward velocity and root bending moment as feedback.

In the lateral channel, we only need to control the flying wing to align with the center of the runway in both the final approach and flare phases, this is accomplished by zero lateral displacement control. Similarly, an outer-loop LADRC controller is used to generate roll angle command for the inner loop, using lateral displacement and lateral speed as feedback. And an inner-loop H_∞ preview controller is employed to generate control inputs (to the corresponding lateral flaps and thrust) with roll angle and twist moment as feedback.

A. Inner-Loop H_∞ Preview Control Design

We now design the inner-loop H_∞ preview controller. Different from conventional H_∞ control design, the preview control design requires augmenting the plant with a delay chain to incorporate the time delay between the measurement of wind and its action on the aircraft. As the wind disturbance is assumed to travel with mean speed [42] from the measurement location to the aircraft, the N -step delay chain Φ for the three-dimensional wind disturbances is modeled as pure delay in the discrete-time state space description,

$$\begin{aligned} x_d(k+1) &= A_d x_d(k) + B_d \hat{d}(k), \\ d(k) &= C_d x_d(k), \end{aligned} \quad (11)$$

where

$$\begin{aligned} A_d &= \begin{bmatrix} 0_{l_d} & I_{l_d} & \cdots & 0_{l_d} \\ \vdots & \vdots & \vdots & \vdots \\ 0_{l_d} & 0_{l_d} & \cdots & I_{l_d} \\ 0_{l_d} & 0_{l_d} & \cdots & 0_{l_d} \end{bmatrix}_{Nl_d \times Nl_d} \\ B_d &= \begin{bmatrix} 0_{(N-1)l_d \times l_d} \\ I_{l_d} \end{bmatrix} \\ C_d &= \begin{bmatrix} I_{l_d} & 0_{l_d \times (N-1)l_d} \end{bmatrix}. \end{aligned}$$

Here \hat{d} is the wind disturbances at the measurement location while d is the wind disturbances that actually act on the aircraft. I_{l_d} is identity matrix with dimension l_d that of the previewable disturbances, and N is the preview length. We choose $N = 40$ in this paper, as a result of the 2-second preview time with the controller sample rate of 0.05 seconds.

We then augment the discrete-time plant model (10) with the delay chain model (11) to incorporate the time delay between measurement of wind and its action, which is expressed as

$$\begin{aligned} \begin{bmatrix} x(k+1) \\ x_d(k+1) \end{bmatrix} &= A_a \begin{bmatrix} x(k) \\ x_d(k) \end{bmatrix} + B_a \begin{bmatrix} \hat{d}(k) \\ u_c(k) \end{bmatrix}, \\ \begin{bmatrix} y(k) \\ \hat{d}(k) \end{bmatrix} &= C_a \begin{bmatrix} x(k) \\ x_d(k) \end{bmatrix} + D_a \begin{bmatrix} \hat{d}(k) \\ u_c(k) \end{bmatrix}, \end{aligned} \quad (12)$$

where

$$A_a = \begin{bmatrix} A_f & B_{fw}C_d \\ 0 & A_d \end{bmatrix}, B_a = \begin{bmatrix} 0 & B_{fu} \\ B_d & 0 \end{bmatrix},$$

$$C_a = \begin{bmatrix} C_f & 0 \\ 0 & 0 \end{bmatrix}, D_a = \begin{bmatrix} 0 & 0 \\ I_{l_d} & 0 \end{bmatrix}.$$

Here A_f, B_{fu}, B_{fw} and C_f are the linear state space matrices of the flying wing model. Note that the wind disturbances $\hat{d}(k)$ now can be regarded as an additional "system output" and be fed into the controller as preview information, which is essentially treated the same as other feedback signals in the H_∞ preview control design process.

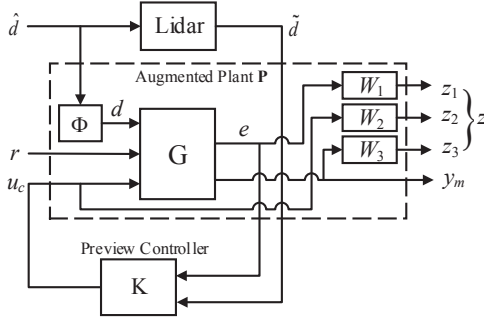


Fig. 8. H_∞ tracking problem with Lidar preview. $\hat{d}, \tilde{d}, d, r, u_c$ denote the remote wind disturbances, wind measurements from Lidar, the wind disturbances actually impact the aircraft, reference command and control inputs, respectively. $z_{i=1,2,3}$ are the performance outputs, y_m is the measurement output. Φ is the N -step delay chain. G and K are the transfer functions of the plant and the preview controller.

As described earlier, the inner loop serves as an aeroelastic control loop for dynamic stabilization and gust load alleviation, and also acts to track the attitude angle command received from the outer loop. Thus, the control design is treated as an H_∞ tracking problem. The mixed sensitivity H_∞ synthesis method is employed, which introduces weighting functions to achieve both good disturbance rejection performance and tracking effectiveness, as shown in Fig. 8. The objective is to find a controller K which minimizes the H_∞ -norm of the transfer function from the future disturbance \hat{d} and the attitude angle command r to the performance output z . Therefore, we further augment the system (12) with weighting functions (rewritten in discrete-time state space description) for H_∞ preview control synthesis, leading to the realization,

$$P = \left[\begin{array}{ccccc|ccc} A_{w1} & 0 & 0 & -B_{w1}C_f & 0 & 0 & B_{w1} & 0 \\ 0 & A_{w2} & 0 & 0 & 0 & 0 & 0 & B_{w2} \\ 0 & 0 & A_{w3} & B_{w3}C_f & 0 & 0 & 0 & 0 \\ 0 & 0 & 0 & A_f & B_{fw}C_d & 0 & 0 & B_{fu} \\ 0 & 0 & 0 & 0 & A_d & B_d & 0 & 0 \\ \hline C_{w1} & 0 & 0 & -D_{w1}C_f & 0 & 0 & D_{w1} & 0 \\ 0 & C_{w2} & 0 & 0 & 0 & 0 & 0 & D_{w2} \\ 0 & 0 & C_{w3} & D_{w3}C_f & 0 & 0 & 0 & 0 \\ \hline 0 & 0 & 0 & -C_f & 0 & 0 & I_r & 0 \\ 0 & 0 & 0 & 0 & 0 & I_{l_d} & 0 & 0 \end{array} \right],$$

where $(A_{wi}, B_{wi}, C_{wi}, D_{wi})$ are the state space matrices of the

weighting functions $W_{i=1,2,3}$, I_r is an identity matrix with dimension that of the reference commands.

As stated in the theory of mixed-sensitivity H_∞ synthesis method, the weighting functions are very crucial to guarantee the controller's performance and robustness. Normally, W_1 should be selected as low pass filter to achieve good tracking performance, while W_2 and W_3 should be selected as high pass filter to achieve good robustness (stability margin). In order to enhance the robust performance and simultaneously achieve good tracking effectiveness, we employ the simulation-based PSO (Particle Swarm Optimization) algorithm to optimize the parameters of the weighting functions. We define the cost function of the algorithm as

$$J = \int_0^t k_1 |e(\tau)| d\tau + k_2 \gamma_{h\infty}, \quad (13)$$

where k_i is the penalty weight, $e(t)$ is the error between the desired step response (pre-defined) and the actual step response, $\gamma_{h\infty}$ is the H_∞ norm of the controller. The first term is used to penalize the tracking error which aims to ensure dynamic tracking performance, while the second is used to penalize the robustness index to guarantee robust performance. A minimum J_{min} is sought through the iterative optimization process, which gives the optimized parameters of the weighting functions. Note that the optimization is based on the reduced-order nonlinear model (9) taking advantage of the quadratic nonlinearity information $Q(x)$ to enhance robustness.

Since the linear model (10) is decoupled in the longitudinal channel and lateral channel, the H_∞ preview controller can be synthesized separately. We use the discrete-time H_∞ synthesis theory proposed in [39] to compute the discrete-time H_∞ preview controller, denoted by K_{lon} and K_{lat} , respectively. In the above discrete-time H_∞ synthesis theory, two discrete-time algebraic Riccati equations (DARE) regarding the Full Information (FI) problem and Output Feedback (OF) problem subject to several conditions are solved,

$$X = A'XA + Q - (L + B'XA)'(R + B'XB)^{-1}(L + B'XA),$$

$$Y = AY A' + T - (M + AY C')(S + CY C')^{-1}(M + AY C'),$$

which results in the discrete-time controller $K = f(X, Y)$. We refer to [39] for definitions of the matrices (Q, R, L, T, M, S) and more details on the algorithm. We mention that the wind measurements \tilde{d} from the Lidar system instead of the ideal wind disturbances \hat{d} are actually provided to the controller as input to make it more realistic, see Fig. 8.

It is also necessary to note that, as stated in [30, 43], the preview controller is essentially a combination of feedforward and feedback controllers, but both parts are designed simultaneously with guaranteed robustness (the H_∞ -norm of the transfer function from the future disturbance and the reference command to the performance output is minimized),

$$K = K_{fb}e + K_{ff}\tilde{d}.$$

where \tilde{d} is the vector of Lidar wind measurements at each preview step, K_{fb} and K_{ff} denote the feedback loop con-

troller and the feedforward loop controller, respectively. As a feedforward loop, the preview action does not affect the stability of the closed-loop system, while the closed-loop stability is ensured by standard H_∞ control synthesis. In this paper, although the Lidar system is used to provide preview information, it can be regarded as a low-pass filter embedded in the feedforward loop, the closed-loop stability is still guaranteed since the feedback loop is independent of the Lidar system.

To demonstrate the robustness of the designed H_∞ preview controller with respect to modeling uncertainties, taking the longitudinal inner-loop controller as an example, we conduct simulations on three full-order nonlinear models (8) with varying bending stiffness EI_2 , namely the 'more' ($0.9EI_2$), 'regular' ($1.0EI_2$) and 'less' ($1.1EI_2$) flexible wings. The preview controller K_{lon} used in the simulations is designed based on the "regular" highly flexible configuration. The corresponding step responses of pitch angle are shown in Fig. 9, where one can see that the control system achieves satisfactory pitch tracking in all three cases. Overshoot is observed in the "more" configuration due to increased flexibility, while a slower response is observed in the "less" configuration due to increased stiffness, compared to the response of "regular" configuration. Fig. 9 indicates good robustness of the designed preview controller with respect to modeling uncertainties.

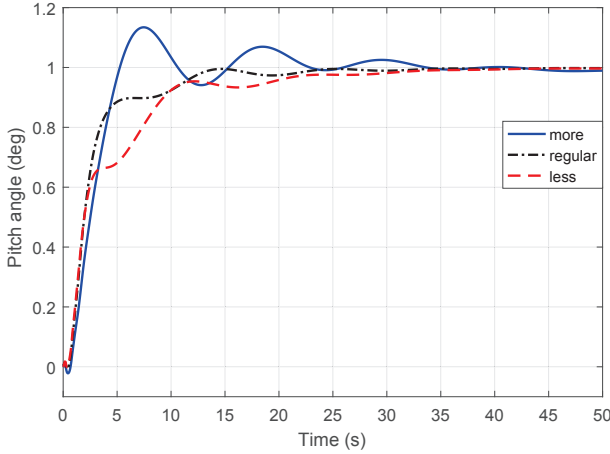


Fig. 9. Pitch responses of the preview control system based on three types of highly flexible configurations with varying bending stiffness.

B. Outer-loop Control Design

As shown in Fig. 7, the outer loop is designed to generate attitude angle command for the inner loop. Here, we use the outer-loop controllers that we developed in [17]. For easy reference, we give a brief introduction.

In the final approach phase, to track the reference landing trajectory, the attitude angle command for the inner loop is regulated by LADRC control. In the longitudinal channel, we regard the altitude motion of the flying wing approximately as a first-order differential equation with altitude H as output and pitch angle θ as input, i.e. $\dot{H} \approx -V\alpha + V\theta$, where V is the airspeed and α is the angle of attack (treated as disturbance). While in the lateral channel, under the assumption of small

perturbations and level flight, we obtain the relation between lateral displacement S and roll angle ϕ approximately as $\ddot{S} \approx V\dot{\psi}_k \approx \frac{L}{m}\phi \approx g\phi$ where ψ_k, L, m and g are the heading angle, the lift force, the mass of aircraft and the acceleration of gravity, respectively. According to the design procedure of LADRC theory, we obtain the dynamic equations of the outer-loop LADRC controller in each channel as

$$\text{lon} : \begin{cases} e_h = z_{1h} - H, \\ \dot{z}_{1h} = z_{2h} - \beta_{1h}e_h + V u_h, \\ \dot{z}_{2h} = -\beta_{2h}e_h, \\ u_{hc} = z_{2h}/V, \\ \beta_{1h} = 2\omega_h, \beta_{2h} = \omega_h^2, \\ u_{h0} = K_{hp} \cdot (H_r - H) + K_{hd}\dot{H}, \\ \theta_r = u_{h0} - u_{hc}, \end{cases} \quad (14)$$

$$\text{lat} : \begin{cases} e_s = z_{1s} - S, \\ \dot{z}_{1s} = z_{2s} - \beta_{1s}e_s, \\ \dot{z}_{2s} = z_{3s} - \beta_{2s}e_s + g u_s, \\ \dot{z}_{3s} = -\beta_{3s}e_s, \\ u_{sc} = z_{3s}/g, \\ \beta_{1s} = 3\omega_s, \beta_{2s} = 3\omega_s^2, \beta_{3s} = \omega_s^3, \\ u_{s0} = K_{sp} \cdot (S_r - S) - K_{sd}\dot{S}, \\ \phi_r = u_{s0} - u_{sc}, \end{cases} \quad (15)$$

where "lon" denotes the longitudinal channel, while "lat" denotes the lateral channel. z_{i*} are the states of ESO (extended state observers), e_* is the error between z_{1*} and the actual value, β_{i*} are the coefficients of ESO determined by parameter w_* . u_{*c} is the compensation value output by ESO, u_{*0} are the virtual control inputs computed by linear control law with the controller parameters K_{*p} and K_{*d} . θ_r and ϕ_r are the pitch angle command and roll angle command for the inner loop, respectively. Please refer to [17] for details.

In the flare phase, for vertical speed control in the longitudinal channel, the pitch angle command is regulated through the PI vertical speed controller, which is simply given as

$$G_{PI}(s) = K_{vp} + \frac{K_{vi}}{s}, \quad (16)$$

where s is the Laplace variable, the gain and the integral parameters K_{vp} and K_{vi} can be simply obtained by tuning. While in the lateral channel, the same controller (15) is used.

V. SIMULATION RESULTS

In this section, we conduct simulation tests based on the full-order nonlinear aeroelastic model (8) to check the performance of the designed preview-based landing control system. The 72m-span highly flexible flying wing model used here is depicted in Fig. 10, detailed configurations can be found in [4]. The airframe has a flat, straight midsection and an outer-section with 10° dihedral. Three vertical fins are placed below the midsection with a payload of 227kg at the central pod (open-loop dynamically unstable). Five propellers are mounted forward of the wing providing thrust while flaps are mounted in the trailing edge of the wing, the control actions are defined

as shown in Fig. 10. A 15-state reduced-order linear model (10) with satisfactory accuracy is obtained from the 1962-state full-order nonlinear model (8) for control design [11]. Measurements are taken at the midpoint of the flying wing as mentioned earlier. The level flight trim condition is at sea level with the speed $V_{trim} = 12.2m/s$ and the corresponding control input settings are $\delta_{1trim} = -0.19^\circ$, $T_{1trim} = 37N$ (all others are zero). The 4th-order Runge-Kutta solver *ode45* in Matlab[®] is used in the nonlinear simulations, and the control inputs are updated at the frequency of 20Hz.

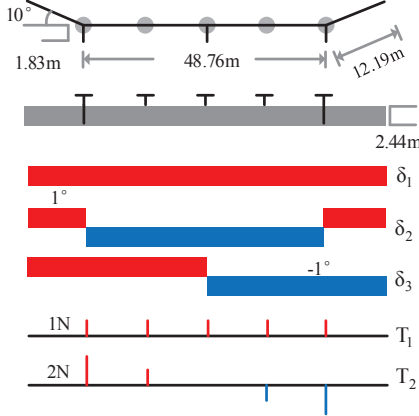


Fig. 10. Geometric configuration and control actions defined on the aircraft: simultaneous flaps (δ_1), symmetric (δ_2) and antisymmetric (δ_3) differential flaps, simultaneous thrust T_1 and differential thrust (T_2).

A. Lidar Wind Measurement

This subsection shows the simulation results of the three-dimensional wind measurements using the Lidar simulator developed in Section III. We generate the continuous three-dimensional turbulent wind field using windSim simulator [44] in Matlab[®] (based on von Kármán velocity spectra). The turbulence scale length and intensity at low altitudes are defined in the reference [45] as,

$$\begin{cases} L_w = h, \\ L_u = L_v = h / (0.177 + 0.000823h)^{1.2}, \\ \sigma_w = 0.1w_{20}, \\ \sigma_u = \sigma_v = 1 / (0.177 + 0.000823h)^{0.4} \sigma_w, \end{cases}$$

where $L_{u,v,w}$ are the scale lengths and $\sigma_{u,v,w}$ are the turbulence intensities, h is reference altitude and w_{20} is the wind speed at 6m. We mention that there are better turbulence models at low altitudes, but the von Kármán model is good enough for test purpose. Fig. 11 shows the sample series of the synthetic turbulence with $h = 5m$ and $w_{20} = 5m/s$ (i.e. $L_w = 5m$, $L_u = L_v = 38.85m$, $\sigma_w = 0.5m/s$, $\sigma_u = \sigma_v = 1m/s$) and the corresponding Lidar wind measurements. It is clear that the Lidar measurements well capture the low frequency components of the wind turbulences, which is due to the low-pass filtering property of the spatial weighting in line-of-sight measurement. Note that in the following simulations, the actual (synthetic) wind turbulence will be applied to the

aircraft while the Lidar wind measurements will be provided to the control system as preview information.

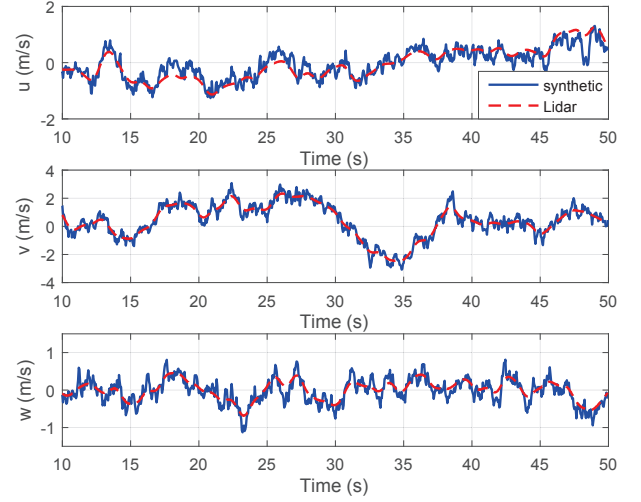


Fig. 11. Sample series of the three-dimensional synthetic turbulence and the corresponding Lidar wind measurements. u , v , w denote the forward, lateral and vertical component of the wind disturbances, respectively. The Lidar wind measurements are time-shifted by 2 seconds to align with the synthetic wind turbulence.

B. Wind Turbulence Response

We assume that the altitudes of the final approach phase starting point and flare phase starting point are $H_0 = 40m$ and $H_1 = 15m$ (see Fig. 1), and the desired vertical speed at touchdown point is $v_{zr} = -0.1m/s$. In the final approach phase, the descent flight path angle (glide ratio) is normally determined by the lift-to-drag (L/D) ratio, which is about 56 for the very flexible flying wing model (8). Therefore, the desired descent flight path angle $\gamma = -atan(D/L) \approx -1^\circ$ is obtained. Now we test the performance of the preview-based landing control system in the presence of wind turbulence. The excitation used is the three-dimensional synthetic von Kármán turbulence generated in Section V-A, of which the lateral component is added with a constant lateral wind of $1m/s$. The turbulence is applied all the way to the touchdown. The flying wing has an initial lateral deviation of 2m. The responses of the flying wing are shown in Fig. 12 and Fig. 13, compared to those of the baseline non-preview landing control system.

It is clear from Fig. 12 that both landing control systems could drive the flying wing to align with the center of the runway and land successfully. The top diagram in Fig. 12 shows that there exist deviations of the touchdown point due to the presence of wind turbulence, compared to the case without turbulence. However, the touchdown deviation with the preview control system are smaller than the case without preview. From Fig. 12, one can also see oscillations in the lateral displacement, vertical speed, pitch angle, roll angle and yaw angle, but the corresponding root-mean-square (RMS) deviations are significantly reduced with the preview-based landing control system by 58%, 28%, 45%, 68% and 71%, respectively, compared to those of the baseline non-preview controller. The bottom two diagrams depict the wing tip displacements relative to the center of the aircraft, which indicate

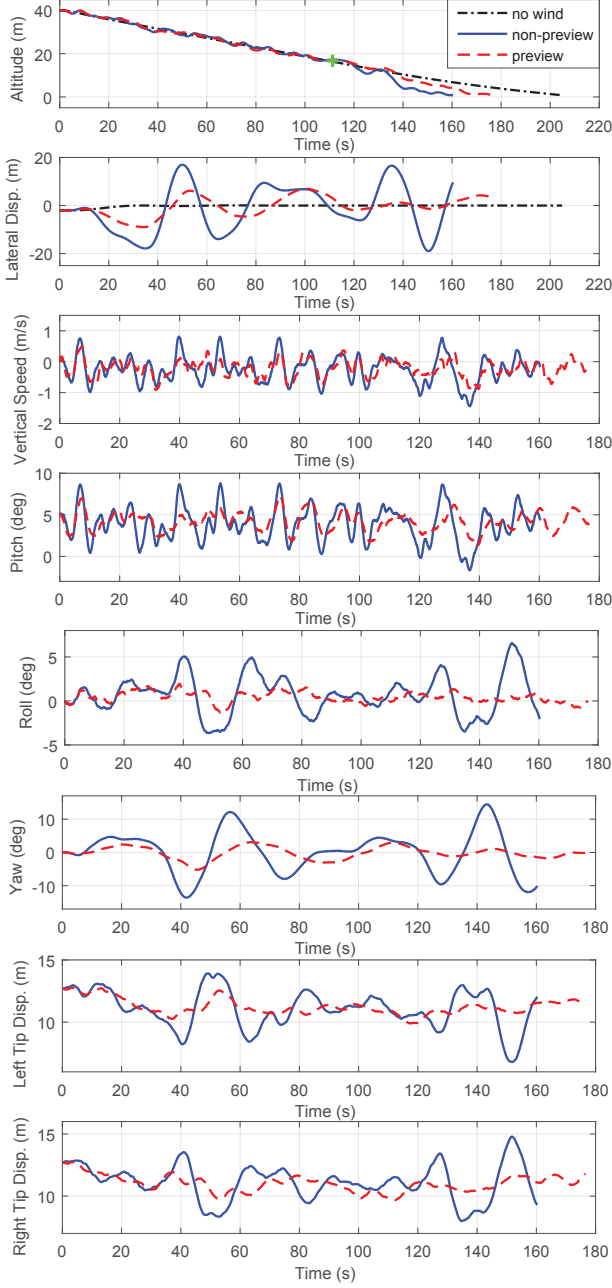


Fig. 12. Time histories of the aircraft responses with the preview-based and non-preview landing control systems respectively in the presence of three-dimensional turbulence. The green cross symbol denotes the flare phase starting point. The altitude response without wind turbulence is also plotted in the top diagram.

a more smooth wing deformations with the preview control system. All these results show that the preview-based landing control system has achieved better landing effectiveness and disturbance rejection performance, which is able to realize more efficient and safer autonomous landing in the presence of wind turbulence. The corresponding control actions are plotted in Fig. 13, where one can see that the preview control system requires smaller control actions than the baseline non-preview controller, by virtue of Lidar preview to enable the control system to act in advance. Note that the negative thrust required in the simultaneous thrust indicates that airbrakes are needed

to actively increase drag during landing (not considered here).

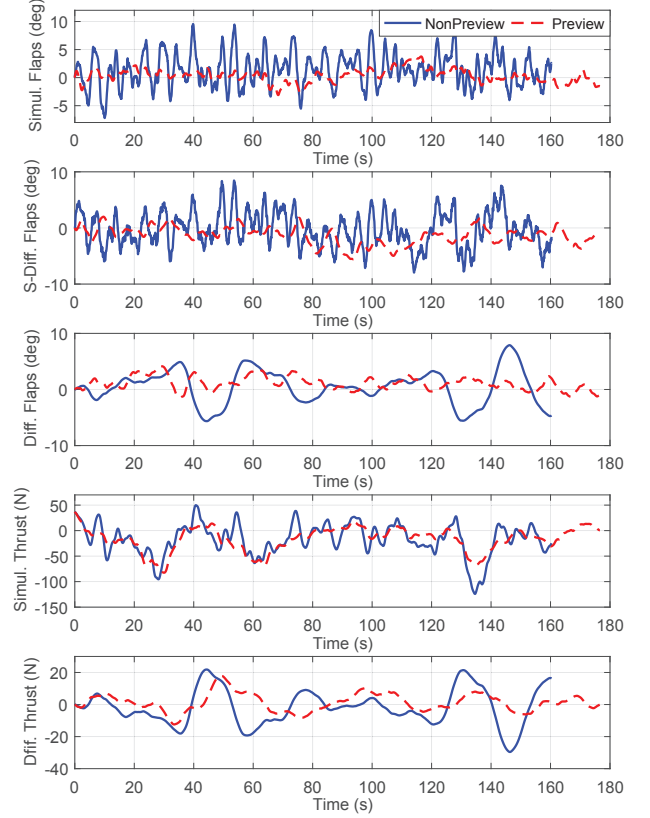


Fig. 13. Time histories of the control actions with the preview-based and non-preview landing control systems respectively in the presence of wind turbulence.

A major advantage of the present aeroelastic formulation is that the modal contributions in (8) are used as primary variables and can be easily analyzed. To show the advantage of the preview control, Table 1 shows the modal energy ($\frac{1}{2}q_{ij}^2$, with $i = 1$ for kinetic energy and $i = 2$ for strain energy of mode j), relative to trim condition of the dominant modes. Results with and without preview are included. The last two columns of Table 1 reveal that the RMS deviations of the modal amplitudes of the rigid-body modes and the dominant flexible modes were all reduced (except Mode 13) at different degrees by preview control. Fig. 14 gives an example of the modal amplitudes of the first symmetric out-of-plane bending mode to illustrate the improvements by preview control.

C. Measurement Noise Analysis

In the above simulations, accurate measurements of the wind velocities are assumed. Now we test the performance of the preview-based landing control system with measurement noise in the Lidar system. The setting up of the above simulation case is considered here with two types of Gaussian white noise added to the measurement outputs (see the top subfigure in Fig. 15) which have the signal-to-noise ratios (SNR) of 15dB and 5dB, respectively. The two sets of noisy measurement outputs are then provided to the preview controller as prior information, respectively. The responses of the flying wing are depicted in Fig. 15. We can see that the

TABLE I
MODAL ENERGY CONTRIBUTIONS AND DEGREES OF PERFORMANCE IMPROVEMENTS BY PREVIEW CONTROL.

Mode No.	Mode Type	q_{1j} no-preview	q_{2j} no-preview	q_{1j} preview	q_{2j} preview
1	Lateral translation	5.5×10^5	-	75%	-
2	Forward translation	4.9×10^5	-	38%	-
3	Vertical translation	2.3×10^4	-	11%	-
4	Pitch rotation	7.2×10^3	-	49%	-
5	roll rotation	3.3×10^4	-	65%	-
6	yaw rotation	2.3×10^5	-	77%	-
7	1st sym. out-of-plane bending	1.9×10^4	7.1×10^5	58%	15%
8	1st asym. out-of-plane bending	1.0×10^3	6.1×10^4	21%	4%
9	1st sym. in-plane bending (Type 1)	5.9×10^3	1.9×10^3	52%	57%
10	1st asym. in-plane bending (Type 1)	1.7×10^2	5.8×10^3	53%	60%
11	2nd sym. out-of-plane bending	9.7×10^2	3.3×10^3	22%	11%
12	1st sym. in-plane bending (Type 2)	2.5×10^2	7.7×10^3	40%	60%
13	2nd asym. out-of-plane bending	1.2×10^2	9.7×10^3	0%	0%
14	3rd sym. out-of-plane bending	3.1×10^2	1.4×10^3	26%	7%
15	1st asym. in-plane bending (Type 2)	2.5×10^1	1.5×10^3	49%	40%
16	1st sym. in-plane bending (Type 3)	2.5×10^1	2.9×10^3	38%	64%
17	3rd asym. out-of-plane bending	1.7×10^1	1.0×10^3	6%	4%

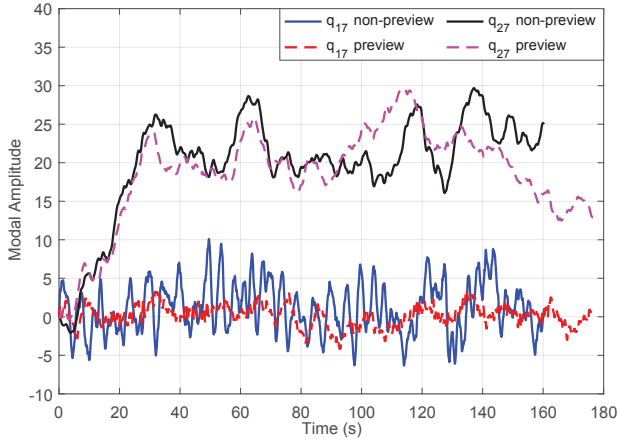


Fig. 14. Modal amplitudes of the first symmetric out-of-plane bending mode with and without preview-based landing control systems in turbulent wind.

performance of the preview control system barely degrades by the noisy measurements. These results indicate the good robustness of the preview control system with respect to preview measurement errors.

VI. CONCLUSIONS

A preview-based autonomous landing control system using a two-loop PI/LADRC and H_∞ preview control scheme has been proposed for a highly flexible flying wing model. The control design was based on a reduced-order linear model (10) which was obtained from a full-order nonlinear aeroelastic model (8) using intrinsic descriptions. A Lidar (light detection and ranging) simulator was developed to measure the wind

disturbances at a distance in front of the aircraft, which were provided to the H_∞ preview controller as prior knowledge to improve control performance. Simulation tests conducted based on the full-order nonlinear model (8), showed that the preview-based landing control system achieved better landing effectiveness and disturbance rejection performance than the baseline landing control system (without preview). The preview control system also achieved good robustness with respect to measurement errors of the preview information. All these have demonstrated that the employment of short range Lidar wind measurements can greatly benefit the autonomous landing of highly flexible aircraft in the presence of wind turbulence.

REFERENCES

- [1] M. J. Patil, D. H. Hodges, and C. E. S. Cesnik, "Nonlinear aeroelasticity and flight dynamics of high-altitude long-endurance aircraft," *Journal of Aircraft*, vol. 38, no. 1, pp. 88–94, 2001.
- [2] F. Silvestre and P. Paglione, "Dynamics and control of a flexible aircraft," in *AIAA Atmospheric Flight Mechanics Conference and Exhibit*, Honolulu, Hawaii, USA, August 2008.
- [3] W. Su and C. E. S. Cesnik, "Dynamic response of highly flexible flying wings," *AIAA Journal*, vol. 49, no. 2, pp. 324–339, 2011.
- [4] M. J. Patil and D. H. Hodges, "Flight dynamics of highly flexible flying wings," *Journal of Aircraft*, vol. 43, no. 6, pp. 1790–1799, 2006.
- [5] T. Gibson, A. Annaswamy, and E. Lavretsky, "Modeling for control of very flexible aircraft," in *AIAA Guidance, Navigation, and Control Conference*, Portland, Oregon, USA, August 2011.
- [6] Z. Qu, E. Lavretsky, and A. M. Annaswamy, "An adaptive controller for very flexible aircraft," in *AIAA Guidance, Navigation, and Control Conference*, Boston, MA, USA, August 2013.
- [7] N. Nguyen and I. Tuzcu, "Flight dynamics of flexible aircraft with aeroelastic and inertial force interactions," in *AIAA Atmospheric Flight Mechanics Conference*, Chicago, Illinois, USA, August 2009.
- [8] A. K. Al-Jiboory, G. Zhu, S. S.-M. Swei, W. Su, and N. T. Nguyen, "Lpv modeling of a flexible wing aircraft using modal alignment and

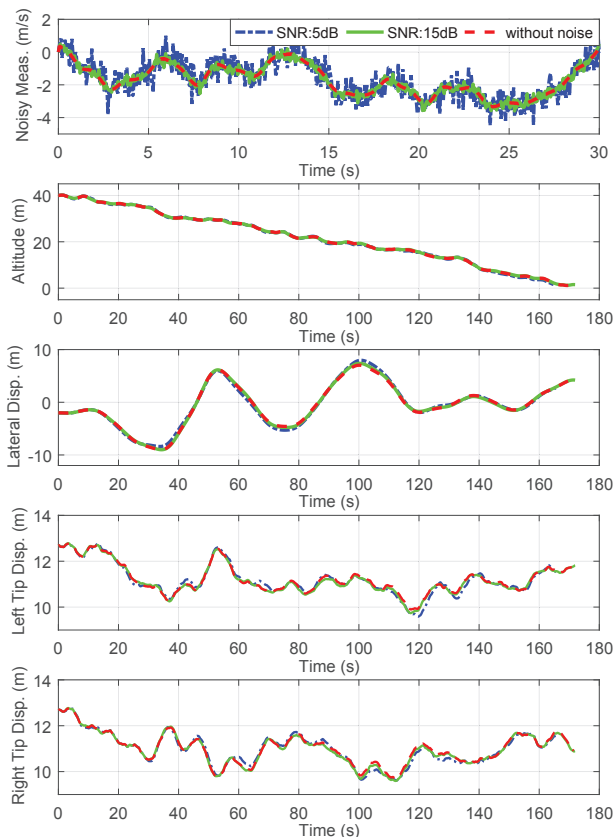
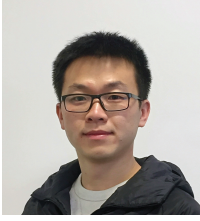


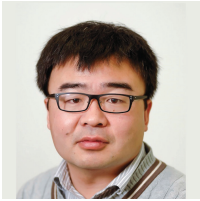
Fig. 15. Time histories of the aircraft responses using noisy Lidar wind measurements as prior information to the preview control system. In the top diagram, only the first 20 seconds of the Lidar wind measurements of the non-stationary crosswind are plotted for better view of the measurement noises.

adaptive gridding methods,” *Aerospace science and technology*, vol. 66, pp. 92–102, 2017.

- [9] N. T. Nguyen, K. Reynolds, E. Ting, and N. Nguyen, “Distributed propulsion aircraft with aeroelastic wing shaping control for improved aerodynamic efficiency,” *Journal of Aircraft*, vol. 55, no. 3, pp. 1122–1140, 2017.
- [10] L. Meirovitch and I. Tuzcu, “Unified theory for the dynamics and control of maneuvering flexible aircraft,” *AIAA journal*, vol. 42, no. 4, pp. 714–727, 2004.
- [11] Y. Wang, A. Wynn, and R. Palacios, “Nonlinear aeroelastic control of very flexible aircraft using model updating,” *Journal of Aircraft*, vol. 55, no. 4, pp. 1551–1563, 2018.
- [12] M. Dillsaver, C. Cesnik, and I. Kolmanovsky, “Gust load alleviation control for very flexible aircraft,” in *AIAA Atmospheric Flight Mechanics Conference*, Portland, Oregon, USA, August 2011.
- [13] R. G. Cook, R. Palacios, and P. Goulart, “Robust gust alleviation and stabilization of very flexible aircraft,” *AIAA Journal*, vol. 51, no. 2, pp. 330–340, 2013.
- [14] Y. Wang, A. Wynn, and R. Palacios, “A nonlinear modal aeroservoelastic analysis framework for flexible aircraft,” *AIAA Journal*, vol. 54, no. 10, pp. 3075–3090, 2016.
- [15] B. Raghavan and M. J. Patil, “Flight control for flexible, high-aspect-ratio flying wings,” *J. Guid. Control Dyn.*, vol. 33, pp. 64–74, 2010.
- [16] M. J. Dillsaver, C. E. Cesnik, and I. V. Kolmanovsky, “Trajectory control of very flexible aircraft with gust disturbance,” in *AIAA Atmospheric Flight Mechanics Conference*, Boston, USA, August 2013.
- [17] P. Qi, X. Zhao, Y. Wang, R. Palacios, and A. Wynn, “Aeroelastic and trajectory control of high altitude long endurance aircraft,” *IEEE Transactions on Aerospace and Electronic Systems*, vol. 54, no. 6, pp. 2992–3003, 2018.
- [18] Boeing, “Statistical summary of commercial jet airplane accidents 1959–2015,” Technical Report, Aviation Safety Boeing Commercial Airplanes, Seattle, Washington, USA, July 2016.
- [19] “Aviation accident final report, NTSB Identification: DCA16CA197,” *National Transportation Safety Board*, June 2016.
- [20] R. Lungu, M. Lungu, and L. T. Grigorie, “Automatic control of aircraft in longitudinal plane during landing,” *IEEE Transactions on Aerospace and Electronic Systems*, vol. 49, no. 2, pp. 1338–1350, 2013.
- [21] N. Sundararajan, P. Sarachandran, and Z. Wang, “Robust neuro-h-controller design for aircraft auto-landing,” *IEEE Transactions on Aerospace and Electronic Systems*, vol. 40, no. 1, pp. 158–168, 2001.
- [22] C. Chen, W.-Q. Tan, X.-J. Qu, and H.-X. Li, “A fuzzy human pilot model of longitudinal control for a carrier landing task,” *IEEE Transactions on Aerospace and Electronic Systems*, vol. 54, no. 1, pp. 453–466, 2018.
- [23] K. Nho and R. K. Agarwal, “Automatic landing system design using fuzzy logic,” *J. Guid. Control Dyn.*, vol. 23, pp. 298–304, 2000.
- [24] H.-J. Rong, N. Sundararajan, P. Saratchandran, and G.-B. Huang, “Adaptive fuzzy fault-tolerant controller for aircraft autoland under failures,” *IEEE Transactions on Aerospace and Electronic Systems*, vol. 43, no. 4, pp. 1586–1603, 2007.
- [25] J. Che and D. Chen, “Automatic landing control using H^∞ control and stable inversion,” in *Proceedings of the 40th IEEE Conference on Decision and Control*, Orlando, Florida, USA, December 2001.
- [26] P. Castillo, L. E. Munoz, and O. Santos, “Robust control algorithm for a rotorcraft disturbed by crosswind,” *IEEE Transactions on Aerospace and Electronic Systems*, vol. 50, no. 1, pp. 756–763, 2014.
- [27] H. Sadat-Hoseini, S. Fazlzadeh, A. Rasti, and P. Marzocca, “Final approach and flare control of a flexible aircraft in crosswind landings,” *J. Guid. Control Dyn.*, vol. 36, no. 4, pp. 946–957, 2013.
- [28] N. Angelou, J. Mann, M. Courtney, and M. Sjöholm, “Doppler lidar mounted on a wind turbine nacelle,” *Spectrum*, 2010.
- [29] G. Teschke and V. Lehmann, “Mean wind vector estimation using the velocity–azimuth display (vad) method: an explicit algebraic solution,” *Atmospheric Measurement Techniques*, vol. 10, pp. 3265–3271, 2017.
- [30] K. Takaba, “A tutorial on preview control systems,” in *SICE 2003 Annual Conference*, Fukui University, Japan, August, 2003.
- [31] J. Laks, L. Pao, A. Wright, N. Kelley, and B. Jonkman, “The use of preview wind measurements for blade pitch control,” *Mechatronics*, vol. 21, no. 4, pp. 668–681, 2011.
- [32] X. Tong and X. Zhao, “Power generation control of a monopile hydrostatic wind turbine using an H^∞ loop-shaping torque controller and an LPV pitch controller,” *IEEE Transactions on Control Systems Technology*, vol. 26, no. 6, pp. 2165–2172, 2017.
- [33] D. Schlipf, D. J. Schlipf, and M. Kühn, “Nonlinear model predictive control of wind turbines using lidar,” *Wind Energy*, vol. 16, no. 7, pp. 1107–1129, 2013.
- [34] G. J. Rabadan, N. P. Schmitt, T. Pistner, and W. Rehm, “Airborne lidar for automatic feedforward control of turbulent in-flight phenomena,” *Journal of Aircraft*, vol. 47, no. 2, pp. 392–403, 2010.
- [35] H. Giessler, M. Kopf, T. Faulwasser, P. Varutti, and R. Findeisen, “Gust load alleviation based on model predictive control,” in *International Forum on Aeroelasticity and Structural Dynamics*, Bristol, UK, June 2013.
- [36] Y. Paku, T. Shimomura, and Y. Hamada, “Gain-scheduled preview control for aircraft gust alleviation,” in *55th Annual Conference of the Society of Instrument and Control Engineers of Japan (SICE)*, Tsukuba, Japan, Sept. 2016.
- [37] Y. Wang, F. Li, and A. Da Ronch, “Adaptive feedforward control design for gust loads alleviation of highly flexible aircraft,” in *AIAA Atmospheric Flight Mechanics Conference*, Dallas, USA, June 2015.
- [38] H. Hesse and R. Palacios, “Dynamic load alleviation in wake vortex encounters,” *Journal of Guidance, Control, and Dynamics*, vol. 39, no. 4, pp. 801–813, 2016.
- [39] M. Green and D. J. Limebeer, *Linear robust control*. Courier Corporation, 2012.
- [40] D. Schlipf, E. Simley, F. Lemmer, L. Pao, and P. W. Cheng, “Collective pitch feedforward control of floating wind turbines using lidar,” *Journal of Ocean and Wind Energy*, vol. 2, no. 4, pp. 223–230, 2015.
- [41] K. Browning and R. Wexler, “The determination of kinematic properties of a wind field using doppler radar,” *Journal of Applied Meteorology*, vol. 7, no. 1, pp. 105–113, 1968.
- [42] G. I. Taylor, “The spectrum of turbulence,” *Proceedings of the Royal Society of London. Series A, Mathematical and Physical Sciences*, vol. 164, no. 919, pp. 476–490, 1938.
- [43] A. Hazell, “Discrete-time optimal preview control,” Ph.D. thesis, The Department of Electrical and Electronic Engineering, Imperial College, London, 2008.
- [44] E. Cheynet, “Wind field simulation (windsim),” <https://uk.mathworks.com/matlabcentral/fileexchange/50041-wind-field-simulation?focused=6398534&tab=function>, last updated June 3, 2016.
- [45] D. Moorhouse and R. Woodcock, “US military specification MIL–F–8785C,” 1980.



Pengyuan Qi received his B.S. degree in automation from University of Science and Technology Beijing, China, in 2013, and the M.S. degree in control science and engineering from Beijing University of Aeronautics and Astronautics, China, in 2016. He is currently pursuing the Ph.D. degree at the University of Warwick, Coventry, UK. His research interests include modeling and flight control of highly flexible aircraft.



Xiaowei Zhao is Professor of Control Engineering at the University of Warwick. He obtained his PhD degree in Control Theory from Imperial College London in 2010. After that he worked as a postdoctoral researcher at the University of Oxford for three years before joining Warwick in 2013. His research interests include (1) Control of fluid-structure interaction with applications to highly flexible aircraft, long-span suspension bridges and large & flexible wind turbines; (2) Control of coupled infinite-dimensional systems; (3) Control of wind turbines/wind farms, grid integration, and energy storage; (4) Microgrid.



Rafael Palacios is the professor of Computational Aeroelasticity at Imperial College, where he started the Load Control and Aeroelastics Laboratory in 2008. He is a fellow of the Royal Aeronautical Society, and Associate Editor of the Journal of Fluids and Structures, the Journal of Aircraft, and Progress of Aerospace Sciences.